Probing the Dynamics of Intraband Electronic Coherences in Cylindrical Molecular Aggregates

Jordan M. Womick, Stephen A. Miller, and Andrew M. Moran*

Department of Chemistry, The University of North Carolina at Chapel Hill, Chapel Hill, North Carolina 27599

Received: December 15, 2008; Revised Manuscript Received: April 16, 2009

Electronic coherence transfer has been detected in only a small number of systems despite the potential impact of these dynamics on natural and artificial light harvesting. Nonlinear spectroscopies designed to probe the dynamics of electronic coherences are challenged by signal emission associated with electronic populations. This paper presents a newly developed nonlinear laser spectroscopy capable of measuring intraband electronic coherences (i.e., for pairs of single exciton states) in molecular aggregates with full suppression of undesired signal components. In comparison with methods applying all-femtosecond laser pulses, the present experiment uses both narrowband and broadband pulses to obtain similar information with a greater than 360-fold faster data acquisition rate. In addition, the technique enhances spectral resolution with experimental control of the measured line widths. High instrument throughput facilitates the comparison of measurements for a wide variety of materials. As the first application of this technique, we investigate the dynamics of intraband electronic coherences in double-walled cylindrical molecular aggregates possessing five slightly different morphologies controlled by varying the solvent conditions. Interfering coherences associated with pairs of exciton states give rise to well-resolved quantum beats in the measured signal fields. In addition, coherence transfer processes are investigated using a superposition of tensor elements (i.e., an analogue of probing population transfer with pump−probe anisotropy). The comparison of experimental measurements and calculations based on a theoretical model supports the finding of coherence transfer processes terminating in an electronic coherence between the inner and outer cylinder excitons.

I. Introduction

Exciton excited states of light-harvesting proteins are generally delocalized over multiple pigments.[1−3] This exciton delocalization reflects the preservation of phase relationships at the individual pigment sites promoted by weak interactions with the surrounding solvent bath.[4−9] Recent experimental[6,10−12] and theoretical[13−18] work investigates how exciton coupling overcomes dephasing processes imposed by system−bath interactions in coherent "wavelike" energy transfer processes. For example, it has been estimated that the wavelike mechanism accounts for more than 20% of the energy transfer efficiency in the Fenna−Matthews−Olson protein of green bacteria.[17,18] The finding of electronic coherences between excitons lasting longer than the corresponding population transfer times is also remarkable.[19−21] These initial observations raised the possibility that coherent energy transfer processes are restricted to biological systems possessing machinery highly optimized through evolution.[6,22] However, similar dynamics were recently detected in a conjugated polymer at room temperature,[11,12] which suggests that coherent energy transfer may even be important in artificial systems.

Experiments capable of probing electronic coherence are challenged by the attainment of adequate time resolution and the suppression of undesired population terms in the polarization response, which can dominate over terms corresponding to electronic coherence. Pump−probe anisotropy experiments are one exception that has proven effective for probing coherence between excited states with large angles between their transition dipoles.[5,7,23] In addition, two-dimensional Fourier transform photon echo experiments detect electronic coherences as quantum beats in diagonal and cross peaks without special requirements regarding transition dipole orientations.[6,8,24−26] However, photon echo experiments investigating the dynamics of electronic coherences must also contend with undesired population terms in the nonlinear polarization. One recent experiment uses a two-color photon echo spectroscopy for isolation of signal components associated with electronic coherence.[22] The present work isolates these same signal components but differs in that it utilizes lasers pulses with different colors and bandwidths. Thus, our technique possesses advantages of both time and frequency domain four-wave mixing spectroscopies. Prospects for this type of experiment were discussed in an earlier investigation exploring optical analogues of heteronuclear multidimensional NMR.[27]

This paper describes the experimental and theoretical aspects of a specialized technique designed to examine intraband electronic coherences in molecular aggregates (i.e., coherences associated with pairs of single exciton states). The experiment uses multiplex array detection for one-step acquisition of intraband coherence spectra. Pulse delays are used to suppress signal contributions arising from improperly ordered field−matter interactions. Another important outcome of this pulse configuration is that the measured intraband coherence line widths are narrower than the inverse of the dephasing rates. This line-narrowing effect is significant because it reduces spectral congestion and facilitates signal interpretation. Data acquisition times of a few seconds are obtained with use of interferometric signal detection and the generation of (synchronized) narrowband and broadband color tunable laser pulses. By contrast, the attainment of equivalent information by a time domain method would require approximately 30 min. Below we show that the ability of this experiment to quickly measure signals under

10.1021/jp811064z CCC: $40.75
Published on Web 05/26/2009

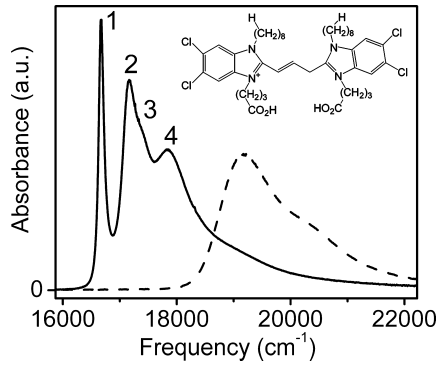

Figure 1. (Dashed) Absorption spectrum of monomer. (Solid) Absorption spectrum of the C8O3 cylindrical molecular aggregate in 0.01 M NaOH. The structure of the monomer is shown in the inset. The relative absorbances for the monomer and aggregate are unrelated.

various experimental conditions has already facilitated a deeper understanding of the C8O3 cylindrical aggregate composed of the monomer shown in Figure 1.

Self-assembled aggregates of C8O3 have been the subject of several experimental[24,28−31] and theoretical studies.[32,33] The absorption spectrum for C8O3 in 0.01 M NaOH exhibits four peaks signifying the double-walled cylindrical structure. The nature of the four electronic transitions has been investigated extensively[28−30] and is understood as follows: (1) the transition at 16 670 cm^{-1} is localized on the inner cylinder; (2) the transition at 17 150 cm^{-1} represents an exciton localized on the outer cylinder; (3) the peak at 17 330 cm^{-1} is more closely associated with the inner cylinder; (4) the highest energy transition at 17 860 cm^{-1} represents an exciton delocalized between the inner and outer cylinder walls (i.e., couples to transitions 1 and 2). Transitions 1, 2, and 4 are thought to have parallel transition dipoles, which are orthogonal to the dipole of transition 3.[34] Below the morphology of C8O3 is varied with control of the concentration of methanol in an aqueous solution. The known correlation between methanol concentration and the aggregate morphology is owed to von Berlepsch et al. who characterized the structures using cryogenic transmission electron microscopy.[30] The aggregate retains its double-walled cylindrical structure at the methanol concentrations used here but increases its diameter to 11 nm, whereas a diameter of 10 nm is found in pure NaOH solution.

Recent applications of photon echo spectroscopy to C8O3 have discovered excited state electronic coherences persisting on the 100 fs time scale.[24,25,31] Milota et al. investigated the dynamics of C8O3 in a mixture of water and octanol, where the aggregate self-assembles into a double-walled cylinder with a linear absorption spectrum dominated by two transitions.[24] Quantum beats were observed in the cross peak corresponding to the two single exciton states followed by population transfer from the higher to lower energy state at longer times. Another photon echo study by the same group examined C8O3 in pure NaOH solution, where the linear spectrum has four single exciton transitions (see Figure 1).[31] Incoherent nonradiative relaxation (i.e., population transfer) within the single exciton manifold was found to proceed with time constants between 109 and 833 fs. The authors observed no evidence of quantum beats in the photon echo measurements. However, our recent photon echo study was able to resolve quantum beats with both 28 and 45 fs periods using laser pulses with broader bandwidths.[25] The present paper more closely examines these intraband coherences by suppressing components of the nonlinear polarization associated with electronic populations.

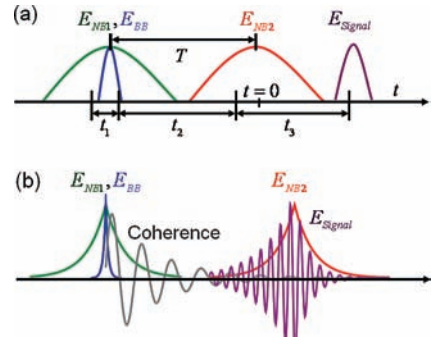

Figure 2. (a) Experimental pulse sequence. E_{NB1} (green) and E_{BB} (blue) are time-coincident, whereas E_{NB2} (red) arrives at the sample after an experimentally controlled delay, T. Intervals between field−matter interactions times are given as t_i. (b) Illustration of model outlined in section II.A. The narrowband (NB1, green) and broadband (BB, blue) pulses interact with the material to produce an electronic coherence (gray) evolving at the frequency ω_{ab}. The signal field (purple) envelope is the product of the envelopes for the electronic coherence and E_{NB2} (red). The signal field frequency is given as the sum $\omega_{NB} + \omega_{ab}$ (eq 8).

II. Theory

A. Multiplexed Probing of Intraband Electronic Coherences. This section develops a simplified model establishing the sensitivity of the present technique to intraband (i.e., single exciton band) electronic coherences in molecular aggregates. Physical insight motivates the use of several approximations, which are later supported by numerical calculations in section II.C. The model identifies experimental conditions that lead to a useful line-narrowing effect. The technique is capable of enhancing the spectral resolution of the intraband electronic coherences beyond the conventional limitations imposed by dephasing rates; the measured line widths can be narrower than homogeneous widths of the intraband resonances.

The fundamental observable in four-wave mixing spectroscopies is the signal field radiated by the sample, which under perfect phase-matching conditions is related to the third-order polarization by

$$E_s(t) = \frac{i2\pi l\omega_t}{n(\omega_t)c} P^{(3)}(t) \tag{1}$$

where $n(\omega_t)$ is the refractive index, l is the sample length, and c is the speed of light. The polarization, $P^{(3)}(t)$, is found by convoluting the material response function with three incoming fields as

$$\begin{aligned} P^{(3)}(t) = \int_0^\infty dt_1 \int_0^\infty dt_2 \int_0^\infty dt_3 \, [R_1(t_1,t_2,t_3) - \\ R_2^*(t_1,t_2,t_3)] E_{NB2}(t-t_3)\, E_{NB1}^*(t+T-t_3-t_2) \times \\ E_{BB}(t+T-t_3-t_2-t_1) + [R_2(t_1,t_2,t_3) - \\ R_1^*(t_1,t_2,t_3)] E_{NB2}(t-t_3) E_{BB}(t+T-t_3-t_2) \times \\ E_{NB1}^*(t+T-t_3-t_2-t_1) \end{aligned} \tag{2}$$

where E_{NB1} and E_{NB2} are "narrowband" pulses, E_{BB} is the broadband pulse, T is the experimentally controlled delay defined in Figure 2a, and t_i are intervals between field−matter interactions. This section focuses on the special case in which $R_i(t_1, t_2, t_3)$ neglects coherence transfer transitions. Expressions for these terms, ${}^0R_i(t_1, t_2, t_3)$, terms valid in the homogeneous limit of line broadening, are given in Appendix A. The superscript "0" [e.g., ${}^0R_i(t_1, t_2, t_3)$] signifies that coherence transfer transitions do not take place. Feynman diagrams corresponding to these four terms are shown in

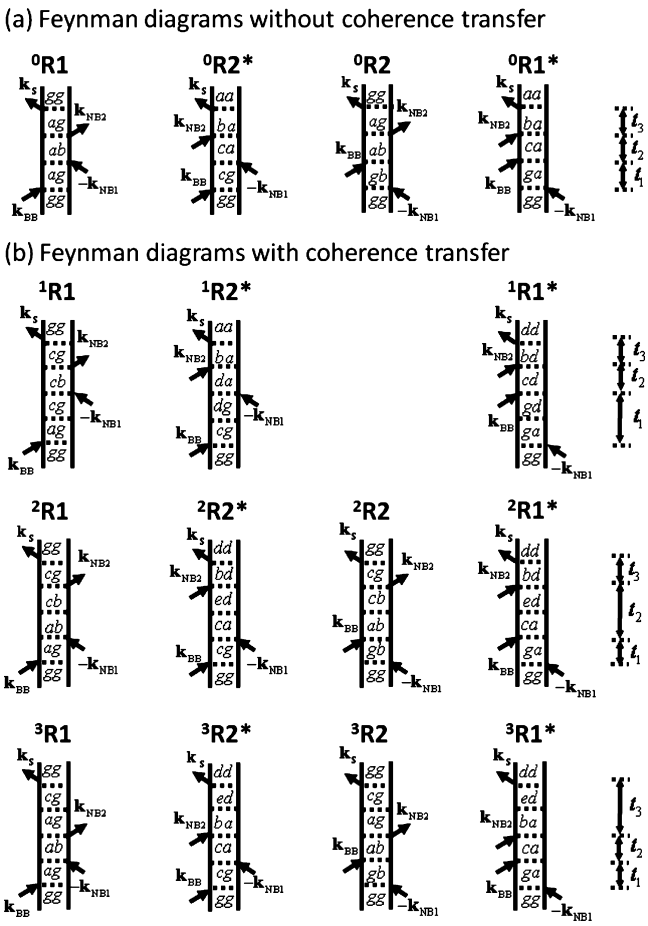

Figure 3. Feynman diagrams describing signal emission in the (a) absence and (b) presence of coherence transfer. The ${}^0R$ terms in (a) do not involve coherence transfer. The response functions, ${}^iR$, in (b) denote coherence transfer transitions in the time interval t_i. Index g represents the ground electronic state, whereas a, b, c, d, and e are dummy indices running over all single and double exciton energy levels. Only resonant terms survive integration of eq 2.

Figure 3a. Additional terms accounting for coherence transfer will be discussed in the following section.

Evaluation of the integrals in eq 2 is simplified with three approximations. Approximation 1 removes the t_i intervals from the arguments of the two narrowband pulse envelopes. This approximation recognizes that the experimental implementation uses narrowband pulses with durations long compared to the dephasing times of the material coherences. Approximation 2 removes the t_1 and t_3 intervals from the argument of the broadband pulse envelope by the same argument as 1. This is generally not a strong approximation when using 20−30 fs broadband pulses but is reasonable here because the experiment is most sensitive to dynamics in t_2, whereas dynamics in t_1 and t_3 contribute indirectly. Approximation 3 assumes the spectral width of the broadband pulse is greater than the material line widths for individual exciton resonances, but not broad compared to the full manifold of single exciton transitions. The envelope of the broadband pulse is then written as a delta function. Additional background on these approximations is given in Chapter 13 of ref 20.

For illustration, we evaluate the polarization component associated with ${}^0R_1(t_1, t_2, t_3)$. For the purpose of integral evaluation, we assume applied fields with double-sided exponential envelopes (i.e., Lorentzian spectra)

$$E_j(t) = \exp(-i\omega_j t - \Lambda_j|t|) \tag{3}$$

This choice of field shape will facilitate the discussion line-narrowing effects below. The ${}^0R_1(t_1, t_2, t_3)$ polarization component is given by

$$P_{R1}^{(3)}(t) = \int_0^\infty dt_1 \int_0^\infty dt_2 \int_0^\infty dt_3\, {}^0R_1(t_1, t_2, t_3) E_{NB2}(t) \times E_{NB1}^*(t + T) \exp[-i\omega_{BB}(t + T - t_3 - t_2 - t_1)] \tag{4}$$

or with ${}^0R_1(t_1, t_2, t_3)$ from Appendix A as

$$\begin{aligned} P_{R1}^{(3)}(t) = \left(\frac{i}{\hbar}\right)^3 \sum_{ab} \mu_{gb}\mu_{ag}\mu_{bg}\mu_{ga} \exp\,[&i\omega_{NB}T \\ &- i\omega_{BB}(t + T) - \Lambda_{NB}|t + T| - \Lambda_{NB}|t|] \times \\ &\int_0^\infty dt_1 \int_0^\infty dt_2 \int_0^\infty dt_3 \theta(t_1)\theta(t_2)\theta(t_3) \times \\ &\exp\,(-i\omega_{ag}t_1 + i\omega_{BB}t_1 - \Gamma_{ag}t_1) \times \\ &\exp\,(i\omega_{ba}t_2 - i\omega_{NB}t_2 + i\omega_{BB}t_2 - \Gamma_{ab}t_2) \times \\ &\exp\,(-i\omega_{ag}t_3 + i\omega_{BB}t_3 - \Gamma_{ag}t_3)\, \delta(t + T - t_2) \end{aligned} \tag{5}$$

where a and b are dummy indices, the summation involves all excited electronic states, and it is assumed that only the ground state, g, is populated at thermal equilibrium.[20,35] Integration of eq 5 yields

$$P_{R1}^{(3)}(t) = \left(\frac{i}{\hbar}\right)^3 \sum_{ab} \mu_{gb}\mu_{ag}\mu_{bg}\mu_{ga}\sigma_{ag}^2(\omega_{BB})\xi_{ab}(t) \tag{6}$$

where

$$\sigma_{ab}(\omega) = \left(\frac{1}{i\omega - i\omega_{ab} - \Gamma_{ab}}\right) \tag{7}$$

and

$$\xi_{ab}(t) = \theta(t + T) \exp[-i\omega_{ab}T - i(\omega_{NB} + \omega_{ab})t - \Gamma_{ab}(t + T) - \Lambda_{NB}|t|] \tag{8}$$

Corresponding expressions for $P_{R2*}^{(3)}(t)$, $P_{R2}^{(3)}(t)$, and $P_{R1*}^{(3)}(t)$ are given in the Supporting Information.

Equation 8 finds that the signal field shape primarily reflects dynamics occurring in the t_2 interval between field matter interactions. The signal frequency is shifted from that of the narrowband pulse, ω_{NB}, by an amount equal to the intraband coherence frequency, ω_{ab}. Furthermore, the signal field duration is governed by the dephasing rates of the intraband coherences, Γ_{ab}. Figure 2b emphasizes the time-domain view of a line-narrowing effect whose frequency domain interpretation is given below. The rising side of E_{NB2}* (at negative t) overlaps with the decay of the $\rho_{ab}(t_2)$ electronic coherence when $T > \Lambda_{NB}^{-1}$. In this configuration, E_{NB2}* is able to sustain the $\rho_{ab}(t_2)$ coherence for an amount of time greater than that imposed by the dephasing rate, Γ_{ab}.

The signal field shape is defined by the Fourier transform

$$\int_{-T}^{\infty} \xi_{ab}(t) \exp(i\omega_t t) = \frac{\exp[-(i\omega_{ab} + \Gamma_{ab})T] - \exp[(-i\omega_t + i\omega_{NB} - \Lambda_{NB})T]}{i\omega_t - i\omega_{ab} - i\omega_{NB} - \Gamma_{ab} + \Lambda_{NB}} - \frac{\exp[-(i\omega_{ab} + \Gamma_{ab})T]}{i\omega_t - i\omega_{ab} - i\omega_{NB} - \Gamma_{ab} - \Lambda_{NB}} \tag{9}$$

The first and second terms on the right side of eq 9 predict the signal bandwidth to be narrower and broader than the pure

homogeneous line width, Γ_{ab}, respectively. When the bandwidth of E_{NB} is much less than the line width of the coherence, we have

$$\int_{-T}^{\infty}\xi_{ab}(t)\exp(i\omega_t t) \approx \frac{-\exp[(-i\omega_t + i\omega_{NB} - \Lambda_{NB})T]}{-i\omega_t + i\omega_{ab} + i\omega_{NB} + \Gamma_{ab} - \Lambda_{NB}} \qquad \Gamma_{ab}/\Lambda_{NB} \gg 1 \tag{10}$$

whereas when $\Gamma_{ab}/\Lambda_{NB} \approx 1$ and the pulse delay, T, is small

$$\int_{-T}^{\infty}\xi_{ab}(t)\exp(i\omega_t t) \approx -\frac{\exp[-(i\omega_{ab} + \Gamma_{ab})T]}{i\omega_t - i\omega_{ab} - i\omega_{NB} - \Gamma_{ab} - \Lambda_{NB}} \qquad \Gamma_{ab}/\Lambda_{NB} \approx 1, T \approx 0 \tag{11}$$

Equation 10 dominates under the experimental conditions defined in section III. The use of delays with $T > \Lambda_{NB}^{-1}$ reduces the spectral width of the signal because Γ_{ab} and Λ_{NB} enter the denominator with opposite signs. This is a key attribute of the present experiment because narrowing of the signal bandwidth reduces spectral congestion and promotes resolution of intraband coherences in multilevel excitonic systems.

B. Modeling Coherence Transfer in the Homogeneous Limit. This section presents a model for the nonlinear spectroscopy introduced in section II.A that accounts for coherence transfer processes in the homogeneous limit of line broadening. Expressions describing coherence transfer between density matrix elements are first presented. The model builds on Redfield theory[19] and an earlier treatment of collisional coherence transfer by Stenholm.[36] Wright and co-workers have captured the main features of their infrared coherence transfer spectroscopy with a similar model.[37,38] These formulas are then used to obtain response functions accounting for coherence transfer in the t_1, t_2, and t_3 intervals between field−matter interactions. Electric field polarization effects are also incorporated.

Coherence transfer dynamics between the density matrix elements, ρ_{ab} and ρ_{cd}, is described by a pair of coupled differential equations

$$\dot{\rho}_{ab}(t) = (-i\omega_{ab} - \Gamma_{ab} - \kappa_{ab,cd})\rho_{ab}(t) + \kappa_{cd,ab}\rho_{cb}(t) \tag{12a}$$

$$\dot{\rho}_{cd}(t) = (-i\omega_{cd} - \Gamma_{cd} - \kappa_{cd,ab})\rho_{cd}(t) + \kappa_{ab,cd}\rho_{ab}(t) \tag{12b}$$

where $\kappa_{ab,cd}$ is the coherence transfer rate corresponding to the transition $\rho_{ab} \rightarrow \rho_{cd}$ and $\kappa_{cd,ab}$ is related to $\kappa_{ab,cd}$ by detailed balance. With the initial conditions, $\rho_{ab}(0) = \rho_{cd}(0)$, we obtain the solutions[36]

$$\rho_{ab}(t) \approx \eta_{cd,ab}[I_{cd}(t) - (1 - \eta_{cd,ab}^{-1})I_{ab}(t)] \tag{13a}$$

$$\rho_{cd}(t) \approx \eta_{ab,cd}[I_{ab}(t) - (1 - \eta_{ab,cd}^{-1})I_{cd}(t)] \tag{13b}$$

where

$$\eta_{ab,cd} = \frac{\kappa_{ab,cd}}{i(\omega_{cd} - \omega_{ab}) + \Gamma_{cd} - \Gamma_{ab}} \tag{14}$$

and the propagation function $I_{ab}(t)$ is given by eq A5. Here it is assumed that only a single coherence transfer transition occurs (e.g., $\rho_{ab} \rightarrow \rho_{cd} \rightarrow \rho_{ef}$ is not allowed) because $\kappa_{ab,cd}$, $\kappa_{cd,ab} \ll \Gamma_{ab}$, Γ_{cd}.

Time evolution of $\rho_{cd}(t)$ is well-described by eq 13b when $t \ll (\kappa_{ab,cd} + \Gamma_{ab})^{-1}$. However, at longer times, the ρ_{ab} coherence decays and no longer feeds ρ_{cd} when $\Gamma_{ab} > \Gamma_{cd}$, which transforms the temporal beats at $\omega_{ab} - \omega_{cd}$ into evolution at the single frequency, ω_{cd}. That is

$$\rho_{cd}(t) \approx (1 - \eta_{ab,cd})I_{cd}(t) \qquad t \gg (\kappa_{ab,cd} + \Gamma_{ab})^{-1} \tag{15}$$

A good approximation to the exact solution of eq 13b is

$$\begin{aligned}\rho_{cd}(t) \approx \eta_{ab,cd}\{&\exp[-(\Gamma_{ab} + \kappa_{ab,cd})t][I_{ab}(t) - (1 - \eta_{ab,cd}^{-1})I_{cd}(t)] \\ &-(1 - \exp[-(\Gamma_{ab} + \kappa_{ab,cd})t])(1 - \eta_{ab,cd}^{-1})I_{cd}(t)\} \approx \\ &\eta_{ab,cd}\{I_{ab}(t)\exp(-\Gamma_{ab}t - \kappa_{ab,cd}t) - (1 - \eta_{ab,cd}^{-1})I_{cd}(t)\}\end{aligned} \tag{16}$$

Equation 16 interpolates between solutions obtained at $t \ll (\kappa_{ab,cd} + \Gamma_{ab})^{-1}$ and $t \gg (\kappa_{ab,cd} + \Gamma_{ab})^{-1}$. We have confirmed that eq 16 agrees with the converged numerical solution of eq 12b. Similar equations can be written for $\rho_{ab}(t)$.

With eq 16, response functions accounting for coherence transfer dynamics can now be obtained. Each of the four diagrams in Figure 3a yields three additional terms corresponding to coherence transfer during each of the three time intervals between field−matter interactions. Feynman diagrams for all terms involving coherence transfer are shown in Figure 3b. The response functions in Appendix B are obtained with eq 16 by defining a new propagation function for the t_i time interval in which coherence transfer occurs

$$K_{ab,cd}(t_i) = \eta_{ab,cd}\Phi_{ab,cd}\{-I_{cd}(t_i) + I_{ab}(t_i)\exp[-(\Gamma_{ab} + \kappa_{ab,cd})t_i]\} \tag{17}$$

where the rule

$$\Phi_{ab,cd} = (1 - \delta_{ab})(1 - \delta_{cd})\{\delta_{ac}(1 - \delta_{bd}) + \delta_{bd}(1 - \delta_{ac}) + (1 - \delta_{ac})(1 - \delta_{bd})\} \tag{18}$$

restricts the summations over dummy indices to coherences (not populations) and also ensures that $\rho_{ab} \neq \rho_{cd}$ in the transition $\rho_{ab} \rightarrow \rho_{cd}$. In summary, the ρ_{cd} density matrix element given by eq 16 can now be restated as

$$\rho_{cd}(t) = I_{cd}(t) + K_{ab,cd}(t) \tag{19}$$

Equation 19 shows that the full response function accounting for coherence transfer in t_i superposes two terms. Appendix B addresses the component of the nonlinear response associated with the $K_{ab,cd}(t_i)$ term on the right side of eq 19. Essentially, the equations in Appendix B are obtained by substituting $K_{ab,cd}(t_i)$ of eq 17 for the corresponding $I_{ab}(t_i)$ function in Appendix A. This straightforward exchange of $I_{ab}(t_i)$ and $K_{ab,cd}(t_i)$ is possible in the limit of fast bath modulation (i.e., homogeneous limit of line broadening) because dynamics occurring in the three time intervals are uncorrelated.[20] For example, the ${}^0R_1$ term evolves according to $I_{ag}(t_1)$ in t_1, whereas ${}^1R_1$ (eq B1) describes coherence transfer in t_1 with substitution of $K_{ag,cg}(t_1)$. The ${}^1R_1$ Feynman diagram in Figure 3b shows that coherence transfers from $\rho_{ag}(t_1)$ to $\rho_{cg}(t_1)$ in t_1. The index a used for the t_2 and t_3 propagations functions in ${}^0R_1$ must then be replaced by index c for ${}^1R_1$. Thus, the products $I_{ag}(t_1)I_{ab}(t_2)I_{ag}(t_3)$ and $K_{ag,cg}(t_1)I_{cb}(t_2)I_{cg}(t_3)$ describe dynamics for the ${}^0R_1$ and ${}^1R_1$ terms, respectively.

Electric field polarization effects are accounted for with bookkeeping of the material dipole with which each of the four fields interacts. Here the notation of ref 39 is used. For example, the orientational component of the term ${}^0R_1$ is given as $\langle\alpha_{bg}\beta_{ga}\gamma_{gb}\phi_{ag}\rangle$, where α, β, γ, and ϕ, respectively, denote the polarizations of the fields, E_{NB1}, E_{BB}, E_{NB2}, and E_S. We use this convention for all terms in the response function regardless of

the order of field−matter interactions. Signal contributions by individual terms can then be discussed on the same footing given a particular lab frame tensor element (e.g., *ZZXX* or *ZXZX*). The ${}^1R_1$ term modifies the tensor notation of ${}^0R_1$ with the substitution $a \rightarrow c$ for all field−matter interactions following coherence transfer. The polarization tensor for ${}^1R_1$ is therefore written as $\langle \alpha_{bg}\beta_{ga}\gamma_{gb}\phi_{cg}\rangle$. Together with the $K_{ab,cd}(t_i)$ propagation function discussed in the previous paragraphs, the ${}^1R_1$ term in the response function is given by

$$ {}^1R_1(t_1, t_2, t_3) = \left(\frac{i}{\hbar}\right)^3 \sum_{abc} \langle \alpha_{bg}\beta_{ga}\gamma_{gb}\phi_{cg}\rangle K_{ag,cg}(t_1) I_{cb}(t_2) I_{cg}(t_3) \tag{20} $$

where a, b, and c are dummy indices running over all excited electronic states. The other terms in Appendix B are found by the same procedure.

The full nonlinear response functions in Appendix C superpose all terms in Appendix B with those associated with the first term on the right side of eq 19. These additional terms radiate signals at times short compared to the inverse of the damping rate, which includes contributions from both dephasing and coherence transfer (i.e., these are the feeding coherences). For generalization to a multilevel system, these feeding coherences must damp according the sum of all coherence transfer channels. Appendix C accounts for these parallel coherence transfer channels with an ad hoc damping parameter, χ_{ab} (see eq C6). A superior model will explicitly solve a quantum master equation without restricting terms to a single coherence transfer within a particular time interval t_i. However, the present model captures the essential photophysics and establishes the information content of the experiment.

C. Model Calculations. Here eq 2 is numerically integrated to explore signatures of coherence transfer in a five-level model system with single exciton electronic structure resembling the C8O3 cylindrical aggregate. The line shapes and transitions dipoles of the model are parametrized for agreement with the spectroscopic measurements discussed in section IV. Calculations will first examine the line-narrowing effect predicted under several approximations in section II.A. We will then define general signatures of coherence transfer in the signal field amplitude, phase, and polarization. Knowledge of these signatures will be used to interpret the measured signals below.

Figure 4a overlays the spectrum of E_{BB} and the E_{NB1} & E_{NB2} pulse pair on the linear absorption spectrum of a five-level model system (see Appendix D). The narrowband pulses are tuned to the lowest energy single exciton transition at 16 667 cm^{-1}, whereas the three higher energy transitions are in resonance with E_{BB}. The parameters of the model system, given in Table 1, are constrained by both the linear and nonlinear experimental measurements discussed in section IV. Coherence transfer rate constants governing dynamics within a particular time interval are fixed to the same value for transitions in which the final coherence possesses a lower frequency than the initial coherence; the detailed balance condition is used to compute rate constants for the reverse processes. This constraint is applied to reduce the total parameter space. It is possible to achieve better agreement with the experimental line shapes by freely varying all coherence transfer rates. However, the present model captures the essential physical insight needed to interpret our data.

Nonlinear signals computed by numerical integration of eq 2 are given in Figure 4c for laser pulses with all-parallel polarizations (i.e., *ZZZZ* tensor element). The signals are computed with $T = 0$, 150, and 300 fs. Comparison of the calculated signals reveals a clear narrowing of the line widths with increasing delay, T, as predicted by section II.A. Also significant is the presence of three peaks corresponding the three excited state electronic coherences in t_2; e_1 forms coherences with the higher energy electronic states, e_2, e_3, and e_4. The dispersed signal reflects a Fourier transform of the dynamics occurring in t_2. The frequencies of the intraband coherences map on to the domain $\omega_t - \omega_{NB}$.

Coherence transfer transitions broaden the line widths of transitions in the linear spectra shown in Figure 5a and b. For this reason, section IV will employ the linear spectra as a constraint for the parametrization of nonlinear response functions

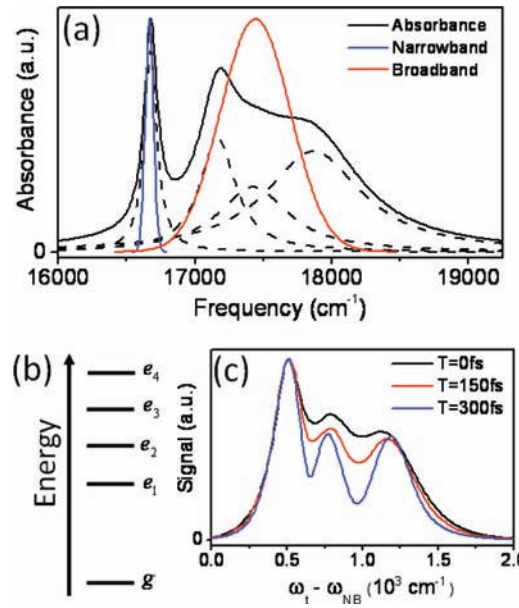

Figure 4. (a) Absorption spectrum (solid) of the five-level model system computed with the parameters in Table 1. Dashed lines decompose the absorption spectrum into the sum of four electronic transitions. Overlayed are spectra of the narrowband (NB1 and NB2, blue) and broadband (BB, red) pulses. (b) Electronic structure of the model system. (c) Nonlinear signal, $|P^{(3)}(\omega_t)|$, computed by numerical integration of eq 2 with the response function given in Appendix C. The frequency, $\omega_t - \omega_{NB}$, is the intraband coherence frequency.

TABLE 1: Parameters of Calculated Signals

parameter	value
$\omega_{NB1} = \omega_{NB2}$	16667 cm^{-1}
ω_{BB}	17442 cm^{-1}
$\tau_{NB1} = \tau_{NB2}{}^a$	210 fs
$\tau_{BB}{}^a$	25 fs
ω_{e1g}	16667 cm^{-1}
ω_{e2g}	17167 cm^{-1}
ω_{e3g}	17427 cm^{-1}
ω_{e4g}	17867 cm^{-1}
Γ_{e1g}	50 cm^{-1}
Γ_{e2g}	90 cm^{-1}
Γ_{e3g}	200 cm^{-1}
$\Gamma_{e4g} = \Gamma_{e2e4}$	270 cm^{-1}
$\Gamma_{e2e3} = \Gamma_{e2e5}$	300 cm^{-1}
$\kappa^{-1}_{e4g,e3g} = \kappa^{-1}_{e4g,e2g} = \kappa^{-1}_{e4g,e1g} = \kappa^{-1}_{e3g,e2g} = \kappa^{-1}_{e3g,e1g} = \kappa^{-1}_{e2g,e1g}$	628 fs
$\kappa^{-1}_{e4e1,e3e1} = \kappa^{-1}_{e4e2,e2e1} = \kappa^{-1}_{e3e1,e2e1}$	32 fs
$\vec{\mu}_{e1g}$	$2.02\hat{x} + 0\hat{y} + 0\hat{z}$
$\vec{\mu}_{e2g}$	$1.45\hat{x} + 2.10\hat{y} + 0\hat{z}$
$\vec{\mu}_{e3g}$	$1.35\hat{x} + 2.34\hat{y} + 0\hat{z}$
$\vec{\mu}_{e4g}$	$2.53\hat{x} + 3.02\hat{y} + 0\hat{z}$
T	300 fs

[a] Full width at half-maximum of Gaussian electric field envelope.

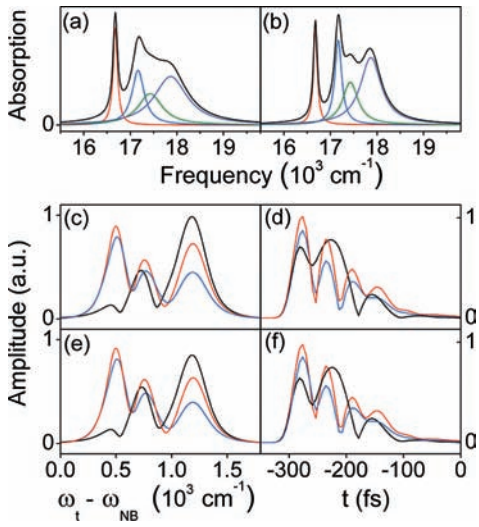

Figure 5. (a) Absorption spectrum (solid) of the five-level model system computed with the parameters in Table 1. Colored lines decompose the absorption spectrum into the sum of four electronic transitions. (b) Absorption spectrum (solid) of the five-level model system computed with the parameters in Table 1, except that all interband coherence transfer rate constants, $\kappa^{-1}_{eig,ejg}$, are equal to zero. Nonlinear signals are computed by numerical integration of eq 2 with the response function given in Appendix C: (c), (e) $|P^{(3)}(\omega_t)|$; (d), (f) $|P^{(3)}(t)|$. Panels (c)−(d) and (e)−(f), respectively, represent the *ZZZZ* and *ZXZX* tensor elements. Calculations are performed with three sets of parameters: (black line) Table 1 except all coherence transfer rates are zero; (red line) Table 1 except all interband coherence transfer rate constants, $\kappa^{-1}_{eig,ejg}$, are equal to zero; (blue line) all parameters of Table 1 are used.

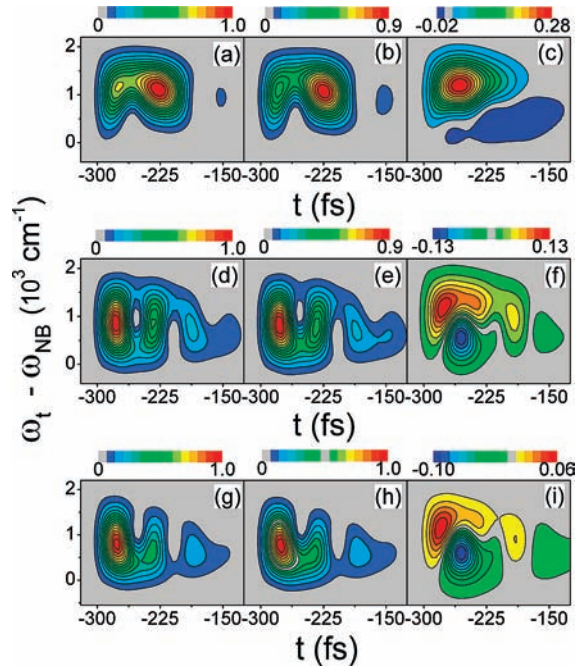

Figure 6. Equation 2 integrated with the response function in Appendix C. Spectrograms are computed with eq 21, where the gate width is equal to 25 fs. Calculations are performed with three sets of parameters: (a)−(c) Table 1 except all coherence transfer rates are zero; (d)−(f) Table 1 except all interband coherence transfer rate constants, $\kappa^{-1}_{eig,ejg}$, are equal to zero; (g)−(i) parameters of Table 1 are used. The first, second, and third columns, respectively, correspond to the *ZZZZ*, *ZXZX*, and *ZZZZ* − *ZXZX* tensor elements.

used for comparison with experiments. Spectral and temporal amplitudes of nonlinear signal fields are given in Figure 5c and d for the *ZZZZ* tensor element. These calculations compare three conditions: no coherence transfer; coherence transfer only in t_2; and coherence transfer in t_1, t_2 and t_3. The neglect of coherence transfer in t_2 has a major effect on the spectral and temporal profiles. The spectral amplitudes skew toward smaller and larger frequencies, $\omega_t - \omega_{NB}$, in the presence and absence of coherence transfer, respectively. Essentially, these calculations reflect the dominance of terms transitioning into lower frequency coherences; the reverse processes contribute more weakly because of detailed balance. By contrast, the absence of coherence transfer in t_1 and t_3 has a relatively minor effect on the signals. In part, this reflects the fact these transitions are taken to be 20 times slower due to constraints imposed by the linear spectrum (see section IV). The temporal amplitudes in Figure 5e give similar information. The presence of multiple spectral peaks manifests as quantum beats between coherences in the time domain, whereas the spectral line widths govern the signal pulse duration. Similar insight is obtained for the *ZXZX* tensor element with the calculations presented in Figure 5e and f.

The calculated temporal profiles in Figure 5d and f show that $P^{(3)}(t)$ begins radiating the signal field immediately after interactions with the E_{NB1} and E_{BB} pulses, which arrive to the sample at $t = -300$ fs. Furthermore, most of the signal emission occurs before the peak of the E_{NB2} pulse has reached the sample at $t = 0$ fs. These calculations show that the time of signal emission is governed by fast dephasing of the intraband coherences under conditions defined by the parameters given in Table 1. In essence, the peak of the time domain signal profiles reflects a compromise between two competing effects: dephasing of the intraband coherences forces signal emission at earlier t; the rise in amplitude of the E_{NB2} pulse forces signal emission at later t. In fact, these two competing factors underlie the line-narrowing effect described by eq 10 and simulated in Figure 4c. Section IV shows that temporal profiles of the measured signal fields agree with the model in that the peaks are found near $t = -300$ fs.

Figure 5 confirms that the signal closely reflects dynamics of the intraband coherences during the t_2 interval as suggested by section II.A. The signal field (i.e., amplitude and phase) possesses both temporal and spectral information on these dynamics with resolution governed by the line width of the narrowest resonance. Spectrograms are a useful representation for complex electric fields and can be calculated with[40−42]

$$S(t, \omega_t) = \left| \int_{-\infty}^{\infty} d\tau \, E_S(\tau) g(t - \tau) \exp(-i\omega_t \tau) \right| \quad (21)$$

where $g(t - \tau)$ is a gate function and $E_S(\tau)$ is the measured signal field. The right side of eq 21 is not squared for enhancement of the weakest features in the signal. The calculations below take $g(t - \tau)$ to be a Gaussian function with a width equal to that of the 25 fs broadband pulse. $S(t, \omega_t)$ essentially decomposes the signal field, $E_S(\tau)$, into individual intraband coherences identified by the detection frequency ω_t (i.e., coherence frequency is $\omega_t - \omega_{NB}$). A slice of $S(t, \omega_t)$ at ω_t informs on the dynamics in t_2 which map onto t by the argument of section II.A.

Signal spectrograms computed with eqs 2 and 21 are given in Figure 6; these calculations use the same six sets of parameters as Figure 5a−d. The first row presents *ZZZZ*, *ZXZX*, and *ZZZZ* − *ZXZX* tensor elements for a system with all coherence transfer rates set equal to zero; parameters are otherwise given by Table 1. The *ZZZZ* and *ZXZX* time-frequency shapes appear quite similar, whereas the difference shows that

the *ZZZZ* element dominates at greater coherence frequencies with a weak negative feature (<2.5% signal amplitude) near $\omega_t - \omega_{NB} = 300$ cm^{-1}. The calculation in the second row additionally allows for coherence transfer in t_2 (not in t_1 or t_3). Detailed balance dictates that coherence transfer transitions shift the signal amplitude in Figure 6d and e toward lower frequencies, $\omega_t - \omega_{NB}$, as time, t, increases (i.e., "chirp" in the signal field phase). This effect is consistent with the spectral skew found in Figure 5c and d. The chirp in the signal field phase is also apparent in Figure 6g and h where coherence transfer is allowed in all three time intervals.

The chirped signal field phase alone may not be a robust signature of coherence transfer, particularly for systems in which coherence transfer dynamics manifest only as weak perturbations. However, coherence transfer dynamics are readily identified by a comparison of tensor elements because the Feynman diagrams in Figure 3a and b interact with different sequences of transition dipoles. For example, parts f and i of Figure 6 exhibit features quite sensitive to coherence transfer dynamics. Specifically, sign changes in the *ZZZZ* − *ZXZX* tensor elements are calculated with negative features 5%−10% of the maximum *ZZZZ* amplitudes (Figure 6d and g). This sign change skews in the direction of the signal chirp: toward lower frequencies, $\omega_t - \omega_{NB}$, and increasing time, t. By contrast, the negative feature in Figure 6c is less than 2% of the *ZZZZ* amplitude in Figure 6a. Line shapes influenced by coherence transfer are also quite different than that in Figure 6c with Figure 6f and i exhibiting a positive feature with a "boomerang" shape.

To summarize, the calculations presented in this section identify two signatures of coherence transfer that will be useful for interpreting experimental measurements. First, the simultaneous fitting of linear and nonlinear signals provides a powerful constraint on the parameters. For example, Figure 5 shows that coherence transfer in t_2 skews the spectral amplitude toward smaller coherence frequencies; this effect should be readily detectable by comparison with nonlinear signals computed using transition dipole magnitudes set by a fit to the linear spectrum. We have also defined signatures of coherence transfer in the signal field shape for the difference in tensor elements, *ZZZZ* − *ZXZX*. In general, coherence transfer skews the time-frequency shape toward increasing t and decreasing $\omega_t - \omega_{NB}$. However, this effect may represent only a small fraction of the total signal. The orientational part of the response can be leveraged for increased sensitivity. The appearance of the *ZZZZ* − *ZXZX* spectrogram depends on the transition dipole orientations, which can be obtained by reproducing the ratio in spectral amplitudes for the two signal fields with further constraints imposed by the linear spectrum. For the present model system, which is motivated by the C8O3 cylindrical aggregate, a sign change in the signal is predicted with increasing t and decreasing $\omega_t - \omega_{NB}$.

III. Experiment

The C8O3 dye molecule shown in the inset of Figure 1 was purchased from FEW Chemicals and used without further purification. Solutions of C8O3 in 10 mM NaOH were diluted with methanol by use of a volumetric pipet to (vol %) concentrations of 0, 5, 10, 13, and 15. At methanol concentrations greater than 15%, absorption of the monomer at 18 870 cm^{-1} becomes comparable to that associated with the aggregate.[30] All solutions were prepared with concentrations giving an absorbance of 0.3 at 16 670 cm^{-1} in a 1 mm path length sample cell. The resulting absorbance spectra reproduce those shown in Figure 1 of ref 30.

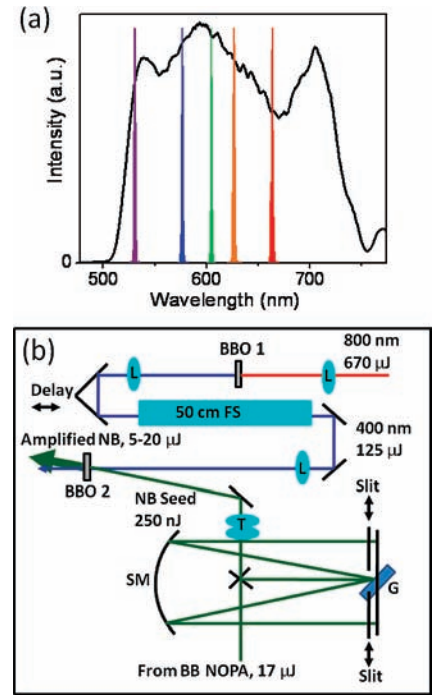

Figure 7. (a) Spectrum for broadband NOPA (black) used to seed NB OPA and typical spectra for tunable amplified NB pulses. (b) Schematic for NB-OPA showing 30 cm focal length lenses (L); telescope composed of 7.5 and −5.0 cm focal length lenses (T); 20 cm focal length spherical mirror (SM); 1200 g/mm grating (G); 50 cm of fused silica glass (50 cm FS); BBO1 is 0.7 mm thick, type I, and $\theta = 29.2°$; BBO2 is 1.5 mm thick, type I, and $\theta = 31.5°$.

Experiments are based on a Quantronix Integra C Titanium Sapphire amplifier producing 120 fs, 800 nm, 2.0 mJ laser pulses at 1 kHz. This laser system pumps two home-built optical parametric amplifiers (OPA) for generation of both broadband and narrowband laser pulses tunable between 500 and 750 nm. The broadband pulses are produced in a standard noncollinear OPA (NOPA)[43−45] in which the 400 nm pump pulses are stretched to 450 fs duration by transmission through a 20 cm fused silica glass block (ESCO Products). Figure 7a shows that the NOPA spectrum spans the 500−750 nm wavelength range. A portion of the full spectrum is filtered in a fused silica prism compressor for use in experiments as the broadband pulse (see section II).

The narrowband OPA (NB-OPA) is seeded with a portion of the broadband NOPA ouput (17 μJ), which is then spectrally filtered in an all-reflective, grating-based compressor aligned for zero dispersion (i.e., a 4F setup) as shown in Figure 7b.[46,47] Translation of the slit position at the 2F plane selects portions of the broadband NOPA spectrum centered at different frequencies with bandwidths as narrow as 20 cm^{-1}. The slit width was set to filter 70 cm^{-1} pulses for the present measurements. Amplification of the (100−250 nJ) narrowband seed pulse without significant spectral broadening requires that the pump pulse duration is greater than or equal to that of the broadband seed.[48,49] Chirped pump pulses with 1 ps durations are obtained by first producing 125 μJ, 400 nm pulses as the second harmonic of the compressed laser fundamental and then stretching the 400 nm pulse by transmission through 50 cm of fused silica. The narrowband seed pulse is amplified in a BBO crystal with the chirped pump pulses using a collinear geometry.

The interferometer shown in Figure 8 resembles earlier nonlinear spectroscopy experiments in that the laser beam geometry is generated with a diffractive optic (DO) for passively

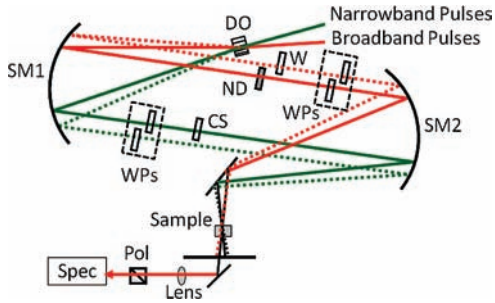

Figure 8. Diffractive optic (DO) based interferometer: 30 cm focal length spherical mirror (SM1); 20 cm focal length spherical mirror (SM2); 2 mm thick BK7 neutral density filter (ND); 2 mm thick fused silica window (W); half-wave plates (WPs); polarizer (Pol); spectrometer (Spec).

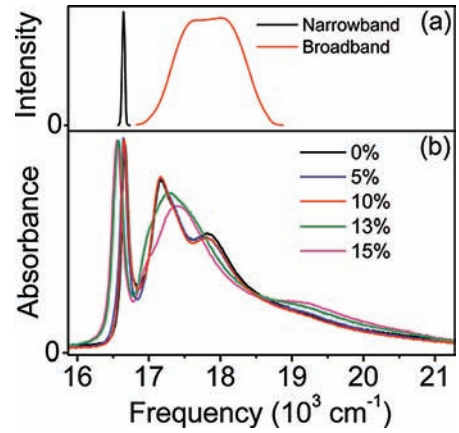

Figure 9. (a) Spectra of narrowband (black) and broadband (red) pulses. (b) Absorption spectra of 0.01 M NaOH solutions of cylindrical aggregates with various (vol %) concentrations of methanol.

phase-stabilized interferometric signal detection.[42,50−57] We use a 1 mm thick fused silica DO producing an angle of 4.5° between the ±1 diffraction orders at 575 nm (Holoeye). The broadband and narrowband laser pulses are spatially overlapped at the DO to produce two pulse pairs. A fused silica glass window and a pair of 175 μm thick microscope coverslips (Fisher Scientific) are placed in the path of the broadband pulse to control its delay with respect to the local oscillator, which is a replica of the broadband pulse (i.e., a different diffraction order). The local oscillator pulse is attenuated with a 2 mm thick BK7 neutral density filter (OD = 3) and arrives at the sample 800 fs before the narrowband pulse. Additional glass coverslips are placed in the E_{NB2} beam path to impart the delay, $T = 300$ fs (see Figure 2). The signal is collinear with the local oscillator after the sample by the $\mathbf{k}_S = -\mathbf{k}_{NB1} + \mathbf{k}_{BB} + \mathbf{k}_{NB2}$ phase matching geometry. Pulse energies at the sample are 5 and 15 nJ for the broadband and narrowband pulses, respectively. Signals are detected in line-binning mode with a back-illuminated CCD array (Princeton Instruments PIXIS 100B) mounted on a 0.3 m spectrograph (Princeton Instruments).

Scattered light from the broadband laser pulse is subtracted by chopping the narrowband pulses with a mechanical shutter and calculating the difference, narrowband pulses on − narrowband pulses off. Each spectrum represents the average of 10 differences with 250 ms integrations times for a total data acquisition time of less than 5 s. The short data acquisition time helps to avoid sample degradation, which is observed after approximately 5 min exposure to the laser pulses. The sample is held in a 1 mm thick cell (0.4 mL) with an open slit top and is gently stirred during the experiment with a piece of inert plastic mounted on an electric toothbrush motor. Under these conditions, we observe no changes in the linear absorption spectra during the course of the experiment.

Phase-resolved signals are obtained with signal detection by spectral interferometry.[41,58,59] This paper detects and processes four-wave mixing signal by the same algorithm used in earlier photon echo[41,53,60] and transient grating experiments.[42] Reference 61 discusses the attainment of passively phase-stabilized signal and local oscillator fields achieved with a similar pulse configuration and interferometer. The Supporting Information provides an example of raw and processed signals.

The quasi-instantaneous nonlinearity of the transparent solvent can give rise to significant signal emission in four-wave mixing spectroscopies when the laser pulses are overlapped in the sample.[62,63] The experiments in this paper use a pulse delay, $T = 300$ fs, with 210 fs narrowband and 25 fs broadband laser pulses. We measure no signal radiated by the quasi-instantaneous nonlinearity of the solvent under these conditions. Raman transitions of the aqueous solvent are also not observed. However, this is not a general result. Raman transitions of solvents with stronger responses (e.g., toluene) are observed with these experimental conditions (see Supporting Information).

Calibration of the absolute phase is particularly difficult because the measurement of different tensor elements requires rotation of the wave plates (see Figure 8), which disrupts the signal phase. In principle, the signal phase for the solutions can be determined by comparison to Raman transitions of the pure solvent (i.e., an internal standard for phase). However, Raman transitions of the aqueous solutions used here are quite weak, which prohibits reliable characterization of the absolute phase. The measurements below examine relaxation dynamics by utilizing the higher order spectral phases measured under different polarization conditions. Knowledge of the absolute phase is not essential to the experimental information content.

IV. Results and Discussion

A. Effect of Methanol on Linear Absorption Spectra of C8O3. Linear absorption spectra of solutions containing various concentrations of methanol are shown in Figure 9. Significant changes in the absorption spectra are observed as the methanol concentration increases from 0% to 15%: transition 1 (see Figure 1) shifts to longer wavelengths; transitions 2−4 are replaced with a single band centered at 575 nm. The morphologies associated with the solvent mixtures were investigated with cryo-transmission electron microscopy and circular dichroism measurements by von Berlepsch et al.[30] The authors found that methanol induces a 1 nm increase in the 10 nm cylinder diameter measured for the pure NaOH solution. It was concluded that methanol causes significant reorganization of the molecules within the cylinder without inducing changes in the overall shape.

B. Effect of Morphology on Nonlinear Response. The spectral and temporal amplitudes shown in Figure 10 correspond to the full measured signals fields; these representations can be regarded as time and frequency integrated, respectively. The spectra are obtained after removing the local oscillator contribution to the measured spectral interferogram, whereas the temporal amplitude is given by a Fourier transform of the measured spectral amplitude and phase.[41,58,59] The similar signal amplitudes found for both the *ZZZZ* and *ZXZX* tensor elements indicate that the transition dipole connecting the ground state to the lowest energy single exciton level is nearly 55° relative to the other single exciton transition dipoles.[39] These transition

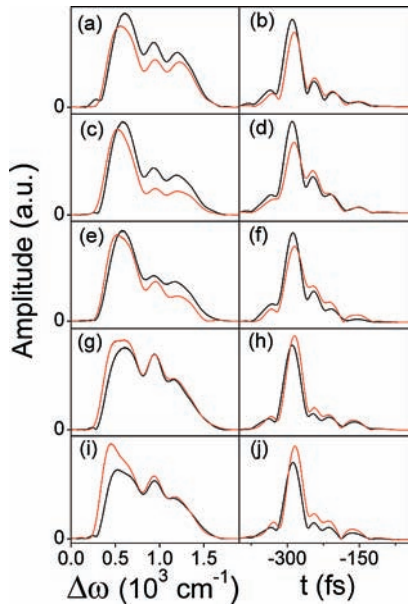

Figure 10. Measured spectral, $|E_S(\omega_t)|$, and temporal, $|E_S(t)|$, signal field amplitudes for the *ZZZZ* (black) and *ZXZX* (red) tensor elements are shown in the left and right columns, respectively. These are amplitudes of the full signal fields (not intensities). $|E_S(\omega_t)|$ and $|E_S(t)|$ can be regarded as time and frequency integrated, respectively. The rows organize data by (vol %) concentrations of methanol: (a)−(b) 0%; (c)−(d) 5%; (e)−(f) 10%; (g)−(h) 13%; (i)−(j) 15%. The frequency axis for the left column is defined as $\Delta\omega = \omega_t - \omega_{NB}$.

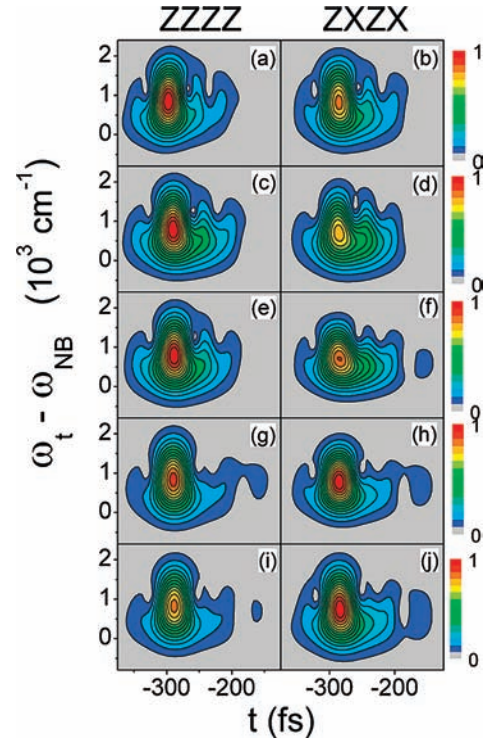

Figure 11. Signal field spectrograms, $S(t, \omega_t)$, measured under the *ZZZZ* (left) and *ZXZX* (right) polarization conditions for 0.01 M NaOH solutions of cylindrical aggregates with various (vol %) concentrations of methanol: (a)−(b) 0%; (c)−(d) 5%; (e)−(f) 10%; (g)−(h) 13%; (i)−(j) 15%.

dipoles were already interpreted as being either parallel or perpendicular to that of the lowest energy transition[34] as required for an ideal cylinder.[33] One explanation for this discrepancy is the helical twisting of multiple tubules;[28] deviation from the straight tubular shape breaks the symmetry that causes the transition dipoles to align either parallel or perpendicular to the long axis of the tube.[33] In addition, the transition dipole orientations were assigned based on experiments for a solution in a flow system, whereas the present measurements stir the solution. It may be that flowing the solution suppresses bundle formation and/or forces straightening of the tubes. We have confirmed that the absorption spectra are robust to sample stirring and that the linear absorption spectrum is independent of the electric field polarization (i.e., isotropic sample).

The spectral amplitudes in the first column of Figure 10 exhibit three peaks representing each of the three coherences between the exciton localized to the inner cylinder (i.e., transition 1 in Figure 1) and those at higher energies. The lowest energy coherence exhibits the strongest response despite the relatively small spectral overlap of the broadband pulse with transition 2 in the linear spectrum (see Figure 9). Figure 10 also shows that increasing the methanol concentration reduces the signal strength for the *ZZZZ* tensor elements compared to *ZXZX*. One clear difference between the simulations in Figure 4 and the experimental spectra in Figure 10 is that they possess resonances at frequencies, $\omega_t - \omega_{NB}$, of 760 and 940 cm^{-1}, respectively. Better agreement with the nonlinear measurement is readily achieved by increasing the value of the parameter ω_{e3g} (see Table 1). However, this worsens the agreement with the linear spectrum. It is possible that the assumption of four exciton states is not adequate for describing the nonlinear measurement. That is, an exciton contributing weakly to the linear spectrum may be involved in particularly long-lived intraband coherences if thermal fluctuations in its energy are correlated with the other exciton states.[22,25] This issue is still under investigation.

The temporal amplitudes in the second column tell a story similar to the spectral amplitudes in the first column. The presence of multiple coherences gives rise to quantum beats in the signal field. These beats are most pronounced for 0% and 5% methanol concentrations. Comparison of the temporal profiles for different tensor elements points to the *t*-dependent polarization effect discussed in section II.C. At low methanol concentrations, the *ZZZZ* amplitude dominates at $t < -260$ fs, whereas *ZXZX* is larger for $t > -260$ fs. The *t*-dependent amplitudes of the different tensor elements mirrors dynamics in t_2 by the argument presented in section II.A.

Spectrograms corresponding to the *ZZZZ* and *ZXZX* tensor elements are shown in Figure 11, where each row represents a different methanol concentration. Differences in the spectrogram shapes are not readily identified by inspection. However, the experimental spectrograms with methanol concentrations <13% exhibit shapes most similar to the calculated spectrograms shown in Figure 6g and h. Specifically, the experimental and calculated spectrograms both possess a "U-shaped" feature near $t = -200$ fs. By contrast, the calculated spectrograms in Figure 6d and e exhibit an upside down U-shaped feature. The parameters used to compute these signals identify this feature as a signature of coherence transfer in the t_1 and t_3 time intervals, where detailed balance again explains the skew toward lower coherence frequencies.

Difference spectrograms, ZZZZ − ZXZX, are presented in Figure 12. At methanol concentrations less than 13%, the measured signals exhibit a sign change similar to that calculated in Figure 6i, where the spectrogram measured for the 10% methanol solution is in best agreement with the calculation. We interpret these data as reflecting coherence transfer for solution with less than 13% methanol concentration. The experiment does not necessarily rule out coherence transfer processes for

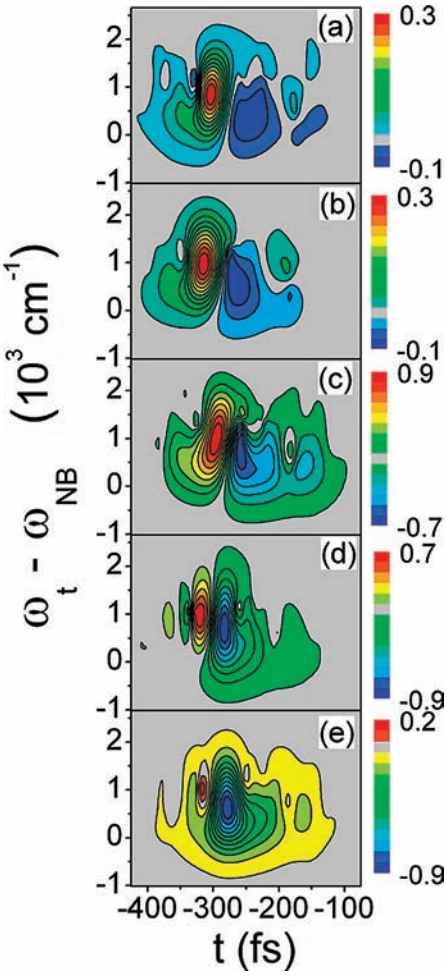

Figure 12. *ZZZZ* − *ZXZX* linear combination of signal field spectrograms for 0.01 M NaOH solutions of cylindrical aggregates with various (vol %) concentrations of methanol: (a) 0%; (b) 5%; (c) 10%; (d) 13%; (e) 15%.

methanol concentrations greater than 10%; fast dephasing may suppress observation of these dynamics. Figure 9 shows that the four distinct single exciton transitions merge into two bands at methanol concentrations greater than 10%. Resolution of the individual single exciton transitions is lost, which could indicate fast dephasing dynamics for this morphology. It is interesting that the line-narrowing capability of the nonlinear technique makes possible the observation of three coherences in Figure 10g and i even though the transition to exciton *e*3 is unresolved in the linear spectrum.

In summary, our assignment of coherence transfer in C8O3 is based on three criteria: (i) resemblance of the calculated and experimental linear spectrum shown in Figure 13a; (ii) agreement between the calculated and experimental spectral amplitudes for the two tensor elements in Figure 13b and c; (iii) the similarity of the measured and calculated spectrogram shapes in Figures 6i and 12a−c. We believe that differences between the calculated and experimental data are mainly due to the model's assumption of homogeneous line broadening. Adding an inhomogeneous component to the line shape of the model system would yield nonlinear signals with broader line widths. The line-narrowing effect predicted in section II.A assumes only homogeneous dephasing in the three intervals between field−matter interactions. The cancellation between Γ_{ab} and Λ_{NB} in the denominator of eq 10 is not obtained when dynamics in the three time intervals are correlated by inhomogeneous line broadening.

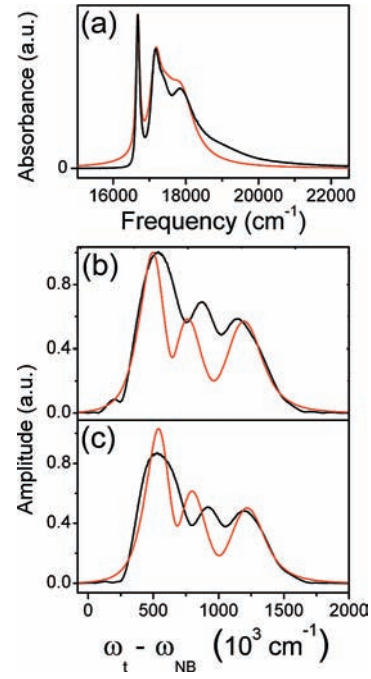

Figure 13. (a) Overlay of measured (black) and calculated (red) linear absorption spectra. Overlay of measured (black) and calculated (red) spectral amplitudes for the (b) *ZZZZ* and (c) *ZXZX* tensor elements. Calculated signals use the parameters of Table 1. The measured signals are for the solution with 0% methanol.

Our model's neglect of vibronic coupling is a strong approximation for the C8O3 aggregate. Most importantly, vibrational resonances are not detected at Raman shifts of 200−3500 cm^{-1} when the narrowband pulse width is reduced to 30 cm^{-1}. Weak vibronic coupling should be expected for C8O3. The exciton states are spatially delocalized such that their excitation produces only minor changes in the charge distribution surrounding localized nuclear modes (e.g., bond-stretching vibrations). For the same reason, the chlorosome of green bacteria possesses a weak Raman response (i.e., small Huang−Rhys factors).[64] The extremely small Stokes shift of C8O3 is also consistent with the view that its delocalized excited states are associated with weak nuclear reorganization.[65]

V. Conclusion

This paper establishes the utility of a specialized nonlinear spectroscopy for investigating the dynamics of intraband electronic coherences in molecular aggregates. The strength of this approach derives from the use of both narrowband and broadband laser pulses, which enables fast data acquisition rates and full suppression of the interfering population response present in conventional pump−probe and photon echo spectroscopies. We have shown this technique to be a viable method for the detection of coherence transfer processes, which are otherwise difficult to measure in complex systems. Methods applying all-femtosecond pulses can additionally resolve the t_1 and t_3 intervals between field−matter interactions, thereby obtaining information to which the present technique is insensitive.[22] However, the use of a narrowband laser pulse allows for superior selectivity of the coherences prepared in t_2. For example, in this paper, the bra side of the density operator is associated with only one excited state because the narrowband pulse overlaps with a single transition in the ground state absorption spectrum. The most appropriate experimental method (i.e., all femtosecond versus mixed narrowband and broadband pulses) is dictated by the particular system and information sought.

Five different morphologies of the C8O3 molecular aggregate produced by varying the concentration of methanol in an aqueous solvent have been investigated. Coherence transfer processes are detected for morphologies associated with methanol concentrations less than 13% (vol %). All coherences probed in this paper have in common an exciton localized on the inner cylinder wall as one component of the superposition of excited states. Future work will examine coherences between pairs of excitons not probed here and explore the information provided by a wider variety of tensor elements. We will also investigate the sensitivity of the present experiment to correlated fluctuations of the individual exciton levels.[25] Ultimately, we aim to establish a complete picture of the electronic structure and relaxation dynamics of the C8O3 molecular aggregate with the information provided by a variety of nonlinear spectroscopies. The present measurements represent an important step toward this goal.

Acknowledgment. A.M.M. acknowledges financial support from the ACS Petroleum Research Fund (Type G) and the R.J. Reynolds Fund for Junior Faculty Development at UNC-CH.

Appendix A. Response Functions in Homogeneous Limit Without Coherence Transfer

This Appendix presents expressions for four terms in the material response function valid in the homogeneous limit of line broadening.[20,35] Feynman diagrams corresponding to these terms are given in Figure 3a. Index g represents the ground electronic state, whereas *a*, *b*, and *c* are dummy indices corresponding to all excited state energy levels.

$$ {}^0R_1(t_1,t_2,t_3) = \left(\frac{i}{\hbar}\right)^3 \sum_{ab} \mu_{ag}\mu_{gb}\mu_{bg}\mu_{ga} I_{ag}(t_1) I_{ab}(t_2) I_{ag}(t_3) \tag{A1} $$

$$ {}^0R_1^*(t_1,t_2,t_3) = \left(\frac{i}{\hbar}\right)^3 \sum_{abc} \mu_{ga}\mu_{cg}\mu_{bc}\mu_{ab} I_{ga}(t_1) I_{ca}(t_2) I_{ba}(t_3) \tag{A2} $$

$$ {}^0R_2(t_1,t_2,t_3) = \left(\frac{i}{\hbar}\right)^3 \sum_{ab} \mu_{gb}\mu_{ag}\mu_{bg}\mu_{ga} I_{gb}(t_1) I_{ab}(t_2) I_{ag}(t_3) \tag{A3} $$

$$ {}^0R_2^*(t_1,t_2,t_3) = \left(\frac{i}{\hbar}\right)^3 \sum_{abc} \mu_{cg}\mu_{ga}\mu_{bc}\mu_{ab} I_{cg}(t_1) I_{ca}(t_2) I_{ba}(t_3) \tag{A4} $$

where

$$ I_{ab}(t) = \theta(t) \exp(-i\omega_{ab}t - \Gamma_{ab}t) \tag{A5} $$

Appendix B. Response Functions in Homogeneous Limit With Coherence Transfer

This Appendix presents response functions corresponding to each Feynman diagram in Figure 3b. Index g represents the ground electronic state, whereas *a*, *b*, *c*, *d*, and *e* are dummy indices running over all excited state energy levels.

$$ {}^1R_1(t_1,t_2,t_3) = \left(\frac{i}{\hbar}\right)^3 \sum_{abc} \langle \alpha_{bg}\beta_{ga}\gamma_{gb}\phi_{cg}\rangle K_{ag,cg}(t_1) I_{cb}(t_2) I_{cg}(t_3) \tag{B1} $$

$$ {}^2R_1(t_1,t_2,t_3) = \left(\frac{i}{\hbar}\right)^3 \sum_{abc} \langle \alpha_{bg}\beta_{ga}\gamma_{gb}\phi_{cg}\rangle I_{ag}(t_1) K_{ab,cb}(t_2) I_{cg}(t_3) \tag{B2} $$

$$ {}^3R_1(t_1,t_2,t_3) = \left(\frac{i}{\hbar}\right)^3 \sum_{abc} \langle \alpha_{bg}\beta_{ga}\gamma_{gb}\phi_{cg}\rangle I_{ag}(t_1) I_{ab}(t_2) K_{ag,cg}(t_3) \tag{B3} $$

$$ {}^1R_2^*(t_1,t_2,t_3) = \left(\frac{i}{\hbar}\right)^3 \sum_{abcd} \langle \alpha_{ag}\beta_{gc}\gamma_{db}\phi_{ba}\rangle K_{cg,dg}(t_1) I_{da}(t_2) I_{ba}(t_3) \tag{B4} $$

$$ {}^2R_2^*(t_1,t_2,t_3) = \left(\frac{i}{\hbar}\right)^3 \sum_{abcde} \langle \alpha_{ag}\beta_{gc}\gamma_{eb}\phi_{bd}\rangle I_{cg}(t_1) K_{ca,ed}(t_2) I_{bd}(t_3) \tag{B5} $$

$$ {}^3R_2^*(t_1,t_2,t_3) = \left(\frac{i}{\hbar}\right)^3 \sum_{abcde} \langle \alpha_{ag}\beta_{gc}\gamma_{cb}\phi_{ed}\rangle I_{cg}(t_1) I_{ca}(t_2) K_{ba,ed}(t_3) \tag{B6} $$

$$ {}^2R_2(t_1,t_2,t_3) = \left(\frac{i}{\hbar}\right)^3 \sum_{abc} \langle \alpha_{bg}\beta_{ga}\gamma_{gb}\phi_{cg}\rangle I_{gb}(t_1) K_{ab,cb}(t_2) I_{cg}(t_3) \tag{B7} $$

$$ {}^3R_2(t_1,t_2,t_3) = \left(\frac{i}{\hbar}\right)^3 \sum_{abc} \langle \alpha_{bg}\beta_{ga}\gamma_{gb}\phi_{cg}\rangle I_{gb}(t_1) I_{ab}(t_2) K_{ag,cg}(t_3) \tag{B8} $$

$$ {}^1R_1^*(t_1,t_2,t_3) = \left(\frac{i}{\hbar}\right)^3 \sum_{abcd} \langle \alpha_{ag}\beta_{gc}\gamma_{cb}\phi_{bd}\rangle K_{ga,gd}(t_1) I_{cd}(t_2) I_{bd}(t_3) \tag{B9} $$

$$ {}^2R_1^*(t_1,t_2,t_3) = \left(\frac{i}{\hbar}\right)^3 \sum_{abcde} \langle \alpha_{ag}\beta_{gc}\gamma_{eb}\phi_{bd}\rangle I_{ga}(t_1) K_{ca,ed}(t_2) I_{bd}(t_3) \tag{B10} $$

$$ {}^3R_1^*(t_1,t_2,t_3) = \left(\frac{i}{\hbar}\right)^3 \sum_{abcde} \langle \alpha_{ag}\beta_{gc}\gamma_{cb}\phi_{ed}\rangle I_{ga}(t_1) I_{ca}(t_2) K_{ba,ed}(t_3) \tag{B11} $$

where $K_{ab,cd}(t)$ and $\Phi_{ab,cd}$ are given by eqs 17 and 18, respectively.

Appendix C. Total Response Function

This appendix presents the total nonlinear response function used to compute signals by numerical integration of eq 2. The use of dummy indices allows application to arbitrary systems (e.g., the model system of Figure 4b). Only resonant terms survive integration of eq 2.

$$ \begin{aligned} R_1(t_1,t_2,t_3) = {} & \left(\frac{i}{\hbar}\right)^3 \sum_{ab} \langle \alpha_{bg}\beta_{ga}\gamma_{gb}\phi_{ag}\rangle \times \\ & \{J_{ag}(t_1) I_{ab}(t_2) I_{ag}(t_3) + I_{ag}(t_1) J_{ab}(t_2) I_{ag}(t_3) \\ & + I_{ag}(t_1) I_{ab}(t_2) J_{ag}(t_3)\} + {}^1R_1(t_1,t_2,t_3) \\ & + {}^2R_1(t_1,t_2,t_3) + {}^3R_1(t_1,t_2,t_3) \end{aligned} \tag{C1} $$

$$ \begin{aligned} R_2^*(t_1,t_2,t_3) = {} & \left(\frac{i}{\hbar}\right)^3 \sum_{abc} \langle \alpha_{ag}\beta_{gc}\gamma_{cb}\phi_{ba}\rangle \times \\ & \{J_{cg}(t_1) I_{ca}(t_2) I_{ba}(t_3) + I_{cg}(t_1) J_{ca}(t_2) I_{ba}(t_3) + \\ & I_{cg}(t_1) I_{ca}(t_2) J_{ba}(t_3)\} + {}^1R_2^*(t_1,t_2,t_3) + \\ & {}^2R_2^*(t_1,t_2,t_3) + {}^3R_2^*(t_1,t_2,t_3) \end{aligned} \tag{C2} $$

$$R_2(t_1,t_2,t_3) = \left(\frac{i}{\hbar}\right)^3 \sum_{ab} \langle \alpha_{bg}\beta_{ga}\gamma_{gb}\phi_{ag}\rangle \times \{J_{gb}(t_1)I_{ab}(t_2)I_{ag}(t_3) + I_{gb}(t_1)J_{ab}(t_2)I_{ag}(t_3) + I_{gb}(t_1)I_{ab}(t_2)J_{ag}(t_3)\} + {}^1R_2(t_1,t_2,t_3) + {}^2R_2(t_1,t_2,t_3) + {}^3R_2(t_1,t_2,t_3) \quad \text{(C3)}$$

$$R_1^*(t_1,t_2,t_3) = \left(\frac{i}{\hbar}\right)^3 \sum_{abc} \langle \alpha_{ag}\beta_{gc}\gamma_{cb}\phi_{ba}\rangle \times \{J_{ga}(t_1)I_{ca}(t_2)I_{ba}(t_3) + I_{ga}(t_1)J_{ca}(t_2)I_{ba}(t_3) + I_{ga}(t_1)I_{ca}(t_2)J_{ba}(t_3)\} + {}^1R_1^*(t_1,t_2,t_3) + {}^2R_1^*(t_1,t_2,t_3) + {}^3R_1^*(t_1,t_2,t_3) \quad \text{(C4)}$$

where

$$J_{ab}(t) = I_{ab}(t)\exp(-\chi_{ab}t) \quad \text{(C5)}$$

and

$$\chi_{ab} = \sum_{cd} \kappa_{ab,cd}\Phi_{ab,cd} \quad \text{(C6)}$$

$\Phi_{ab,cd}$ is given by eq 18.

Appendix D. Calculating Linear Absorption Spectra With Coherence Transfer

The linear absorption spectra, $\varepsilon(\omega)$, in Figures 4, 5, and 13 are calculated with

$$\varepsilon(\omega) = \sum_a |\mu_{ag}|^2 \mathrm{Re}\int_0^\infty \mathrm{d}t \exp[i(\omega - \omega_{ag})t - \Gamma_{ag}t - \chi_{ag}t] \quad \text{(D1)}$$

where χ_{ag} is given by eq C6.

Supporting Information Available: R_2, R_1^*, and R_2^* terms in response function found under approximations of section II.A. Example of raw signals and discussion of the solvent response. This information is available free of charge via the Internet at http://pubs.acs.org.

References and Notes

(1) Blankenship, R. E. *Molecular Mechanisms of Photosynthesis*; Blackwell Science Ltd.: Oxford, 2002.
(2) Lawlor, D. *Photosynthesis*, 3rd ed.; Springer-Verlag: New York, 2001.
(3) Falkowski, P. G.; Raven, J. A. *Aquatic Photosynthesis*; Blackwell Science: Malden, MA, 1997.
(4) Pullerits, T.; Chachisvilis, M.; Sundström, V. *J. Phys. Chem.* **1996**, *100*, 10787.
(5) Arnett, D. C.; Moser, C. C.; Dutton, P. L.; Scherer, N. F. *J. Phys. Chem. B* **1999**, *103*, 2014.
(6) Engel, G. S.; Calhoun, T. R.; Read, E. L.; Ahn, T. K.; Mancal, T.; Cheng, Y. C.; Blankenship, R. E.; Fleming, G. R. *Nature* **2007**, *446*, 782.
(7) Savikhin, S.; Buck, D. R.; Struve, W. S. *Chem. Phys.* **1997**, *223*, 303.
(8) Parson, W. W. *Science* **2007**, *316*, 1438.
(9) Book, L. D.; Ostafin, A. E.; Ponomarenko, N.; Norris, J. R.; Scherer, N. F. *J. Phys. Chem. B* **2000**, *104*, 8295.
(10) Sugisaki, M.; Fujiwara, M.; Yanagi, K.; Cogdell, R. J.; Hashimoto, H. *Photosynth. Res.* **2008**, *95*, 299.
(11) Collini, E.; Scholes, G. D. *Science* **2009**, *323*, 369.
(12) Collini, E.; Scholes, G. D. *J. Phys. Chem. A* **2009**, *113*, 4223.
(13) Kleinekathöfer, U.; Schröder, M.; Schreiber, M. *J. Lumin.* **2005**, *112*, 461.
(14) Cheng, Y. C.; Silbey, R. J. *Phys. Rev. Lett.* **2006**, *96*, 028103:1.
(15) Olaya-Castro, A.; Lee, C. F.; Olsen, F. F.; Johnson, N. F. *Phys. Rev. B* **2008**, *78*, 085115:1.
(16) Mancal, T.; Valkunas, L.; Read, E. L.; Engel, G. S.; Calhoun, T. R.; Fleming, G. R. *Spectroscopy* **2008**, *22*, 199.
(17) Mohseni, M.; Rebentrost, P.; Lloyd, S.; Aspuru-Guzik, A. *J. Chem. Phys.* **2008**, *128*, 174106:1.
(18) Rebentrost, P.; Mohseni, M.; Kassal, I.; Lloyd, S.; Aspuru-Guzik, A. *New. J. Phys.* **2009**, *11*, 033003:1.
(19) Redfield, A. G. *Adv. Magn. Reson.* **1965**, *1*, 1.
(20) Mukamel, S. *Principles of Nonlinear Optical Spectroscopy;* Oxford University Press: New York, 1995.
(21) Nitzan, A. *Chemical Dynamics in Condensed Phases*; Oxford University Press: New York, eq C6.
(22) Lee, H.; Cheng, Y.-C.; Fleming, G. R. *Science* **2007**, *316*, 1462.
(23) Qian, W.; Jonas, D. M. *J. Chem. Phys.* **2003**, *119*, 1611.
(24) Milota, F.; Sperling, J.; Nemeth, A.; Kauffman, L. J. *Chem. Phys.*, in press.
(25) Womick, J. M.; Miller, S. A.; Moran, A. M. *J. Phys. Chem. B* **2009**, *113*, 6630.
(26) Cho, M. *Chem. Rev.* **2008**, *108*, 1331.
(27) Pakoulev, A. V.; Rickard, M. A.; Meyer, K. A.; Kornau, K. M.; Mathew, N. A.; Thompson, D. E.; Wright, J. C. *J. Phys. Chem. A* **2006**, *110*, 3352.
(28) Kirstein, S.; Däehne, S. *Int. J. Photoener.* **2006**, 1.
(29) von Berlepsch, H.; Böttcher, C.; Ouart, A.; Burger, C.; Däehne, S.; Kirstein, S. *J. Phys. Chem. B* **2000**, *104*, 5255.
(30) von Berlepsch, H.; Kirstein, S.; Böttcher, C. *Langmuir* **2002**, *18*, 7699.
(31) Nemeth, A.; Milota, F.; Sperling, J.; Abramavicius, D.; Mukamel, S.; Kauffman, L. J. *Chem. Phys. Lett.* **2009**, *469*, 130.
(32) Didraga, C.; Puglys, A.; Hania, R.; von Berlepsch, H.; Duppen, K.; Knoester, J. *J. Phys. Chem. B* **2004**, *108*, 14976.
(33) Knoester, J. *Int. J. Photoener.* **2006**, 1.
(34) von Berlepsch, H.; Kirstein, S.; Hania, R.; Didraga, C.; Pugl̆ys, A.; Böttcher, C. *J. Phys. Chem. B* **2003**, *107*, 14176.
(35) Abramavicius, D.; Mukamel, S. *Chem. Rev.* **2004**, *104*, 2073.
(36) Stenholm, S. *J. Phys. B: At. Mol. Opt. Phys.* **1977**, *10*, 761.
(37) Rickard, M. A.; Pakoulev, A.; Mathew, N. A.; Kornau, K. M.; Wright, J. C. *J. Phys. Chem. A* **2007**, *111*, 1163.
(38) Pakoulev, A.; Rickard, M. A.; Mathew, N. A.; Kornau, K. M.; Wright, J. C. *J. Phys. Chem. A* **2008**, *112*, 6320.
(39) Dreyer, J.; Moran, A. M.; Mukamel, S. *Bull. Korean Chem. Soc.* **2003**, *24*, 1091.
(40) Mukamel, S. *J. Chem. Phys.* **1997**, *107*, 4165.
(41) Gallagher, S. M.; Albrecht, A. W.; Hybl, J. D.; Landin, B. L.; Rajaram, B.; Jonas, D. M. *J. Opt. Soc. Am. B* **1998**, *15*, 2338.
(42) Moran, A. M.; Maddox, J. B.; Hong, J. W.; Kim, J.; Nome, R. A.; Bazan, G. C.; Scherer, N. F. *J. Chem. Phys.* **2006**, *124*, 194904:1.
(43) Cerullo, G.; Nisoli, M.; De Silvestri, S. *Appl. Phys. Lett.* **1997**, *71*, 3616.
(44) Riedle, E.; Beutter, M.; Lochbrunner, S.; Piel, J.; Schenkl, S.; Spörlein, S.; Zinth, W. *Appl. Phys. B* **2000**, *71*, 457.
(45) Kobayashi, T.; Baltuska, A. *Meas. Sci. Technol.* **2002**, *13*, 1671.
(46) Martinez, O. E. *J. Opt. Soc. Am. B* **1986**, *3*, 929.
(47) Goodman, J. W. *Introduction to Fourier Optics*, 3rd ed.; Roberts & Company: Greenwood Village, CO, 2005.
(48) Ishibashi, T.; Onishi, H. *Appl. Phys. Lett.* **2002**, *81*, 1338.
(49) Shim, S.; Mathies, R. A. *Appl. Phys. Lett.* **2006**, *89*, 121124:1.
(50) Cowan, M. L.; Ogilvie, J. P.; Miller, R. J. D. *Chem. Phys. Lett.* **2004**, *386*, 184.
(51) Goodno, G. D.; Dadusc, G.; Miller, R. J. D. *J. Opt. Soc. Am. B* **1998**, *15*, 1791.
(52) Maznev, A. A.; Nelson, K. A.; Rogers, J. A. *Opt. Lett.* **1998**, *23*, 1319.
(53) Brixner, T.; Mancal, T.; Stiopkin, I. V.; Fleming, G. R. *J. Chem. Phys.* **2004**, *121*, 4221.
(54) Khurmi, C.; Berg, M. A. *J. Phys. Chem. A* **2008**, *112*, 3364.
(55) Underwood, D. F.; Blank, D. A. *J. Phys. Chem. A* **2003**, *107*, 956.
(56) Gundogdu, K.; Stone, K. W.; Turner, D. B.; Nelson, K. A. *Chem. Phys.* **2007**, *341*, 89.
(57) Kim, J.; Wong, C. Y.; Nair, P. S.; Fritz, K. P.; Kumar, S.; Scholes, G. D. *J. Phys. Chem. B* **2006**, *110*, 25371.
(58) Lepetit, L.; Chériaux, G.; Joffre, M. *J. Opt. Soc. Am. B* **1995**, *12*, 2467.
(59) Tokunaga, E.; Terasaki, A.; Kobayashi, T. *J. Opt. Soc. Am. B* **1995**, *12*, 753.
(60) Hybl, J. D.; Albrecht Ferro, A.; Jonas, D. M. *J. Chem. Phys.* **2001**, *115*, 6606.
(61) Moran, A. M.; Nome, R. A.; Scherer, N. F. *J. Phys. Chem. A* **2006**, *110*, 10925.
(62) Christensson, N.; Dietzek, B.; Pascher, T.; Yartsev, A.; Pullerits, T. *Chem. Phys. Lett.* **2008**, *457*, 106.
(63) Oskouei, A. A.; Bräm, O.; Cannizzo, A.; van Mourik, F.; Tortschanoff, A.; Chergui, M. *J. Mol. Liq.* **2008**, *141*, 118.
(64) Cherepy, N. J.; Du, M.; Holzwarth, A. R.; Mathies, R. A. *J. Phys. Chem.* **1996**, *100*, 4662.
(65) Pugl̆ys, A.; Augulis, R.; van Loosdrecht, P. H. M.; Didraga, C.; Malyshev, V. A.; Knoester, J. *J. Phys. Chem. B* **2006**, *110*, 20268.

JP811064Z